ACS APPLIED MATERIALS & INTERFACES

RESEARCH ARTICLE

www.acsami.org

Inherently Reproducible Fabrication of Plasmonic Nanoparticle Arrays for SERS by Combining Nanoimprint and Copolymer Lithography

Sivashankar Krishnamoorthy,[*,†] Sathiyamoorthy Krishnan,[§] Praveen Thoniyot,[*,‡] and Hong Yee Low[†]

[†]Institute of Materials Research and Engineering (IMRE), Agency for Science, Technology and Research (A*STAR), 3, Research Link, 117602, Singapore

[§]School of Mechanical and Aerospace Engineering, Nanyang Technology University (NTU), 639815, Singapore

[‡]Singapore Bioimaging Consortium (SBIC), Agency for Science, Technology and Research (A*STAR), Helios #02-02,11, Biopolis Way, 138667, Singapore

S *Supporting Information*

ABSTRACT: We present an inherently reproducible route to realizing high-performance SERS substrates by exploiting a high-throughput top-down/bottom-up fabrication scheme. The fabrication route employs self-assembly of amphiphilic copolymers to create high-resolution molds for nanoimprint lithography (NIL) spanning entire 100 mm Si wafers. The nanoporous polymer templates obtained upon NIL are subjected to galvanic displacement reactions to create gold nanorod arrays. Nanorods are subsequently converted to nanodiscs by thermal annealing. The nanodiscs were found to perform as robust SERS substrates as compared with the nanorods. The SERS performance of these substrates and its generality for catering to diverse molecules is demonstrated through the excellent Raman peak resolution and intensity for three different molecules, exhibiting different interaction modes on surface. Numerical simulations using FDTD shows plasmonic coupling between the particles and also brings out the influence due to size distribution. The approach combines distinct advantages of high-precision and repeatability offered by NIL with low-cost fabrication of high-resolution NIL molds by copolymer self-assembly.

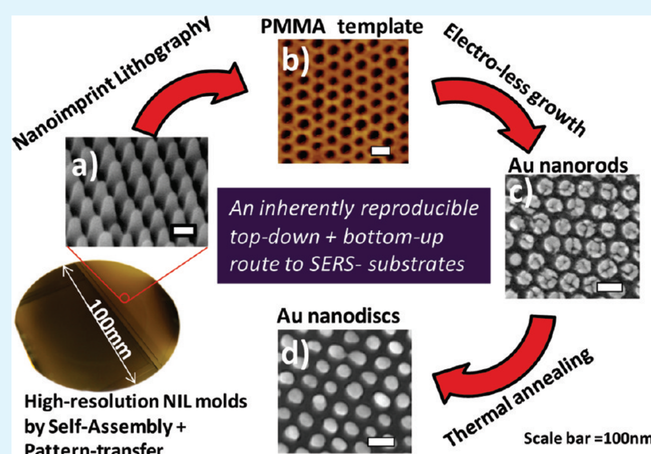

KEYWORDS: nanofabrication, nanoimprint lithography, SERS, block copolymer, plasmonic array, nanorods, nanodiscs

INTRODUCTION

Plasmonic nanoarrays are recognized to be of high value in disparate application areas such as biosensing, waveguides, photovoltaics and photocatalysis. These applications benefit from the size, shape, separation or local dielectric environment-dependent optical properties exhibited by metallic nanostructures and their assemblies.[1−4] Of particular interest is the exploitation of plasmonic near-field effects for highly sensitive molecular detection using techniques such as localized surface plasmon resonance (LSPR)[5,6] and surface enhanced Raman scattering (SERS).[4] SERS is particularly known for its high sensitivity toward detection down to single molecule level under optimal conditions.[7,8] Application of SERS is envisaged in diverse analytical platforms such as disease diagnosis, environmental monitoring, forensic and defense applications. However, challenges in consistency and reproducibility in SERS signals across or between batches of substrates has often limited the wider applicability of SERS as a routine analytical tool.[9,10] The reproducibility of SERS signals can be significantly improved by ensuring the uniformity and reproducibility during the nanofabrication. In this work, we demonstrate an inherently reproducible means of achieving high-performance and low-cost SERS substrates by combining a high throughput top-down and bottom-up technique.

The several approaches reported in literature for creating SERS substrates can be classified into two major categories, namely, continuous metal films exhibiting high-roughness surface[11−13] or discrete nanoparticle arrays.[14−18] Continuous metal interfaces with high surface roughness benefit from enhanced electrical field intensities arising at sharp corners or at junctions of randomly formed protrusions. On the other hand, the use of discrete nanoparticle arrays provides excellent opportunity for design and engineering of the geometric variables (e.g., size, geometry, proximity and distribution) to tailor optical properties toward maximizing the SERS enhancements. Another important advantage is the ease of modeling to predict optical response of the discrete particle assemblies. Fabrication of such discrete nanoparticle arrays suitable for SERS has been shown earlier using bottom-up approaches, viz. nanosphere lithography (NSL),[17,19] Anodized alumina templates

Received: November 23, 2010
Accepted: March 4, 2011
Published: March 04, 2011

 © 2011 American Chemical Society

(AAO),[14,15,20]and block copolymer lithography (BCL).[18] NSL suffers from the challenge of in-homogeneity of close-packed nanosphere assemblies particularly when pattern-resolutions <100 nm are sought. Use of AAO technique faces challenge of manipulating free-standing AAO templates or collapse/bundling of high-aspect-ratio metal structures upon template removal. On wire lithography using AAO templates has shown to have several distinct advantages over the conventional AAO-based metal particle formation.[20] However, excellent spatial uniformity achievable for nanoparticles is restricted only within individual wires. Achieving lateral uniformity over macroscopic length scales of even few square micrometers on chip as necessary for device applications has not yet been demonstrated using this approach. Nanoparticle substrates for SERS shown earlier using block copolymer lithography exhibit broad size distributions.[18] In general, despite the significant gain in throughput offered by the self-assembly approaches, there has often been a dire need to counter the lack of uniformity and reproducibility.

The top-down fabrication is well-suited to address this problem, as it offers both high-precision and repeatability. However, top-down techniques face the challenge of low-throughput and/or high cost when targeting pattern-resolutions in the sub-100 nm regime. The state-of-the-art in top-down techniques in catering to these scales include, direct-write techniques such as lithography using e-beam, focused ion-beams or surface-probe methods, X-ray interference, double exposure patterning with deep UV radiation, nanostencils, and nanoimprint lithography (NIL). Among these, NIL is particularly recognized as a potentially low-cost solution for fabricating nanoscale templates with feature resolutions down to sub-10 nm regime.[21,22] NIL also allows for considerable flexibility in the choice of substrates, the choice of polymer used for template formation, making it highly versatile. However, NIL is a secondary patterning tool that relies on other top-down techniques to produce hard-molds that are suitable for replication. This step makes NIL inherit the cost-based disadvantages associated with the fabrication of high-resolution NIL molds often by direct-write techniques like e-beam. Fabricating high-resolution NIL molds using self-assembly processes, e.g., AAO,[23−27] NSL,[28−30] or copolymers,[31,32] therefore serves as a cost-effective solution. Among all these different bottom-up routes, the use of a copolymer self-assembly is particularly attractive, due to its CMOS compatibility. More importantly, block copolymers offer several handles (e.g., molecular weight, block ratios, number of blocks, solvent quality, coating conditions)[33,34] for tweaking the molecular self-assembly process to realize NIL molds with the fine-tunable geometric characteristics. Moreover, the typical aspect ratios in the NIL molds obtained using copolymers are well-suited to create nanoimprinted templates with aspect ratios in the range of 5−10, which is desired in most device applications. Use of molds with significantly higher aspect ratio features, e.g. using AAO, to produce small aspect ratio imprinted features will lead to significant nonuniformity in heights of the imprinted features.

However, to obtain dot-array patterns with copolymer self-assembly in thin films requires several processing steps such as substrate pre-treatment, annealing, and post-processing to achieve etch-contrast for nanolithography. Therefore we choose the use of reverse micelles of amphiphilic copolymers for creating high resolution NIL molds. The process is particularly advantageous over the reported block copolymer lithography based NIL molds shown earlier,[32,35] because of its ready and efficient scalability for producing Si molds spanning complete wafer in only two steps, viz. spin-coating of an optimized reverse micelle solution and subsequent pattern transfer.[36]

It should be noted that the pattern-formation using reverse micelles is fundamentally different from that of copolymer phase-separated thin films in bulk or on surfaces. The pattern-formation using reverse micelles[37] involves a two-step process: First step involves self-assembly of amphiphilic copolymer molecules in solution to form the soft micelle nanoparticles, and the second step involves the 2D pattern formation when the micelles are deposited on the surface. The feature size of the templates is determined by the diameter of the polymer particles in the solution phase, which in turn depends on the micelle aggregation number. The aggregation number can be tweaked, either by using a polymer with different molecular weight, or by suitable choice of solvents. The periodicity of the patterns obtained on surface is determined both by the hydrodynamic size of the micelles in solution as well as the coating conditions, viz. solution concentration or coating speed employed. The lowest array periodicities attained on surface is close to the hydrodynamic diameter of the micelles in solution. The array periodicity can however be systematically increased from this value by at least 20% by controlling the deposition conditions employed.[36] Such ability to tweak the feature size and periodicity of the resulting patterns independently, and without necessarily having to vary the molecular weight of the polymer is one of the distinct advantages offered by the reverse micelle route to nanopatterning.

RESULTS AND DISCUSSION

Preparation and Characterization of Au Nanorod and Nanodisc Arrays. The protocol describing the high-resolution mold preparation using copolymer self-assembly and their use in NIL process to obtain gold nanorod and nanodiscs arrays is shown in Scheme 1. The process starts with the deposition of spherical reverse micelles formed of an amphiphilic copolymer in a non polar solvent. This results in a quasi-hexagonal 2D array of polymeric islands spread over the entire coated area. These arrays can be obtained with typical length scales of 50−200 nm for feature width and spacing with standard deviations <10% in the different geometric variables (feature width, periodicity and heights). The mass thickness contrast offered by the polymeric islands can be exploited for pattern-transfer into underlying Si substrate by dry etching processes. This way, Si nanopillar arrays with an aspect ratio of 5−6, exhibiting a shape (e.g., conical, cylinder, Gaussian, parabola) as determined by the dry-etching parameters, and pattern-resolutions identical to that of the original template can be achieved. The feature width of the Si pillars and their periodicity can be controlled through the choice of conditions employed for micelle nanopattern formation. In a recent work, we have shown that this process can be readily exploited to create Si nanopillar arrays down to sub-50 nm pattern resolutions with high uniformity across 100 mm wafers.[36]

Thus attained Si pillars are subsequently exploited as molds in a standard NIL process to obtain nanoporous templates in a resist through replication. PMMA is a commonly chosen as resist for NIL because of its excellent film forming behavior. However, a wide variety of other polymers such as polycarbonate and polyvinylpyridine can also be used with adequate optimization. The NIL process always leaves behind a thin film of residual resist between the mold and the substrate. The residual resist layer removal to expose the substrate beneath the troughs is necessary for nanopattern formation by templated growth or deposition of

Scheme 1. (Left) Steps Employed to Fabricate High-Resolution Molds for Nanoimprint Lithography (NIL) Using Self-Assembled Amphiphilic Copolymer Micelles, and (Right) The Use of High-Resolution NIL to Create Au Nanorods and Nanodiscs Arrays[a]

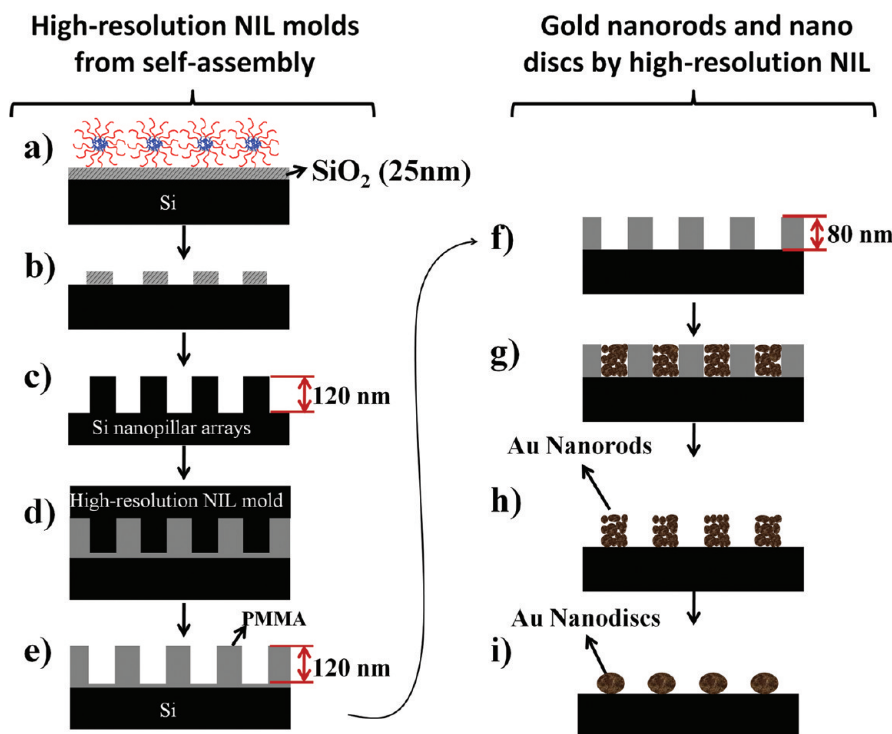

[a] (a) reverse micelles arrays of polystyrene-block-poly(2-vinylpyridine) deposited on Si substrate with 25 nm thermal oxide layer (b) SiO_2 nanoparticle masks formed by pattern-transfer of reverse micelle templates (cf. experimental) (c) Si nanopillar arrays obtained upon pattern-transfer into Si substrate using SiO_2 particles as hard-masks (d,e) silicon nanopillar arrays as high-resolution molds for NIL using PMMA as imprint resist to obtain (e) Nanoporous PMMA templates (f) nanoporous templates with Si substrate exposed beneath pores, after residual layer removal (g) Au nanorod arrays obtained by selective electro-less growth within PMMA templates (h) nascent Au nanorod arrays obtained after removal of PMMA by O_2 plasma and (i) Au disc arrays obtained upon thermal annealing of Au nanorod arrays.

materials. The residual layer can be readily removed by an anisotropic O_2 plasma etching. Nanopattern of metals, semiconductors, or grafted polymers can be achieved using such templates targeting a variety of applications, e.g., to create light-extraction structures in LEDs, charge storage centers in non-volatile memory devices, metal structures for LSPR biosensors, nanostructured electrodes for bulk heterojunctions solar cells and batteries, or nanoporous membranes for sensing/filtration devices.

The development of uniform reverse micelle based templates for nanolithography with sub-50 nm feature resolutions was performed as reported in our recent work.[36] In a typical experiment, reverse micelle arrays of polystyrene-block-poly(2-vinylpyridine) (PS-b-PVP, molecular weight 80.5 kDa, $f_{PS} \approx 0.5$) from m-Xylene solutions were deposited on 100 mm Si wafer to obtain 2D quasi-hexagonally ordered features with width of ∼56 nm and periodicity of 80 nm. The coating conditions were optimized such that the coefficient of variation in the mean values for size and periodicity the arrays was less than 5% across the complete wafer. The optimal spin-coating condition was found to be 5000 rpm spin speed, at acceleration of 5000 rpm/s, at solution concentration of 0.6%. The quality of spatial ordering in the 2D arrays was analyzed through radial distribution function (also known as pair correlation function). The radial distribution function reveals lateral ordering in the arrays that extends to a distance equivalent to 10 times the average periodicity. This indicates an average area of $\sim 2\ \mu m^2$ for the ordered domains. The size of the ordered domains was also found to be sensitive to the coating conditions, reducing significantly for films coated at lower spin-speeds. These optimized arrays were subsequently transferred into underlying Si substrate using dry etching following a two step pattern-transfer as reported earlier in literature (cf. experimental).[32] Si nanopillar arrays with an aspect ratio of ∼6 spanning 100 mm wafers was achieved this way (Figure 1a). SEM analysis reveals a positively tapered pillar profile with a diameter of 40 nm (at mid height, or ∼65 nm at the base) and height of 120 nm (Figure 1b,c). The uniformity of the pillar arrays were further confirmed to exhibit a variation of <5% in geometric characteristics (viz. height, diameter, and periodicity) using reflectance spectroscopy performed at different points from center to edge of the wafer.

The wafer was diced into smaller pieces of 1.5 cm × 1.5 cm dimensions and used for the imprinting experiments. Prior to imprinting, the Si pillar array substrates were treated with 1H,1H,2H,2H- perfluorododecyl trichlorosilane in vapor phase in order to benefit from the ultralow surface energies offered by perfluoro coatings that bestow excellent antistiction property to the molds, enabling an easy release after imprinting. The imprinting using Si pillar molds onto polymethyl methacrylate as resist was carried out employing a commercial nanoimprinter (Figure 1d). The cross-sectional SEM images show ∼120 nm deep pores, and with the residual layer beneath the pores estimated to be ∼10 nm (Figure 1e). Following the removal of

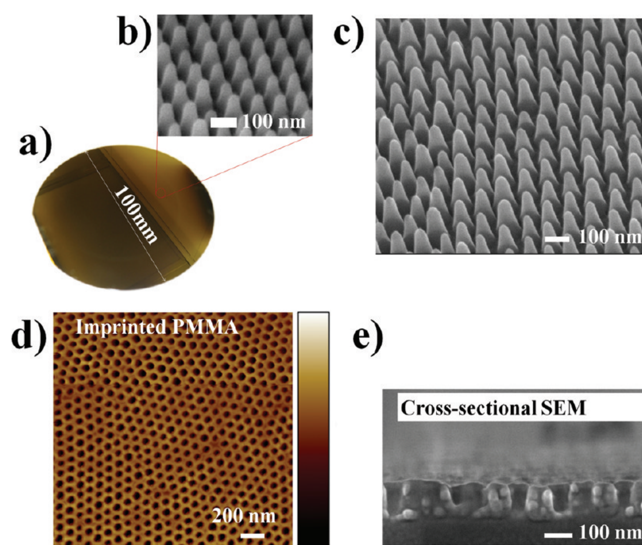

Figure 1. (a) Picture of 100 mm Si wafer containing nanopillar arrays used as NIL mold. The uniformity of nanopillar arrays can be perceived from its uniform color (the reflection of the ceiling is seen within the wafer). SEM image of the high-resolution Si pillar mold measured at 45° tilt is shown at (b) high and (c) low magnifications. (d) Tapping mode AFM image of the PMMA templates obtained upon NIL using high-resolution molds shown in b. (e) SEM cross-section of the imprinted PMMA template showing pores that are ~120 nm deep. The pore heights appear smaller when the line of cleavage does not cut across the center of the pore.

residual layer by O_2 plasma, the templates were exposed to BHF solution for 30s to ensure removal of native silicon oxide and expose bare silicon.

The electroless growth of gold was carried out in a solution mixture containing 2.3 mM $HAuCl_4$ and 0.9% HF using a protocol demonstrated earlier by Aizawa et al.[38,39] The electroless deposition occurs through the in situ reduction of Au(III) ions in solution to Au(0) driven by the oxidation of silicon in the presence of HF. The immersion of templates into the plating bath for duration of 1 min was sufficient to create discrete and well-defined gold nanorods. Gold nanorod growth was found to be selectively occurring within the pores with no observed overgrowth and exhibiting high uniformity within the imprinted area as evidenced by SEM measurements (Figure 2). It is important to note that any pillar height variations of even a few nanometers in the Si molds would result in variation in the residual layer thickness underneath the pores. This would be challenging for two reasons: (1) the residual layer removal step would expose the Si substrate only within some pores, thereby decreasing the yield of nanorods, also affecting the pattern-fidelity; and (2) the O_2 plasma duration can be increased in order to ensure complete opening of the polymer within all the pores. However, such over-exposure also reduces the template heights and broadens the pore diameters. Therefore, the residual layer thickness removal needs to be optimized, taking into account the size distribution in Si pillar heights. From SEM measurements, we estimate a standard deviation of <5% for the pillar heights. The maximum defect density introduced in the nanorod array due to this height variation was estimated to be ~2.6 missing rods/μm^2 (Figure 2a). The PMMA template was subsequently removed by O_2 plasma RIE step, to obtain arrays of gold nanorods, with 80 nm height as perceived from SEM cross-section analysis. Upon annealing the substrate containing nanorods at 200 °C for 2 h, transformation into disc-like morphology is observed. This rod-to-disc morphology change is expected to be caused because of compacting of a porous,

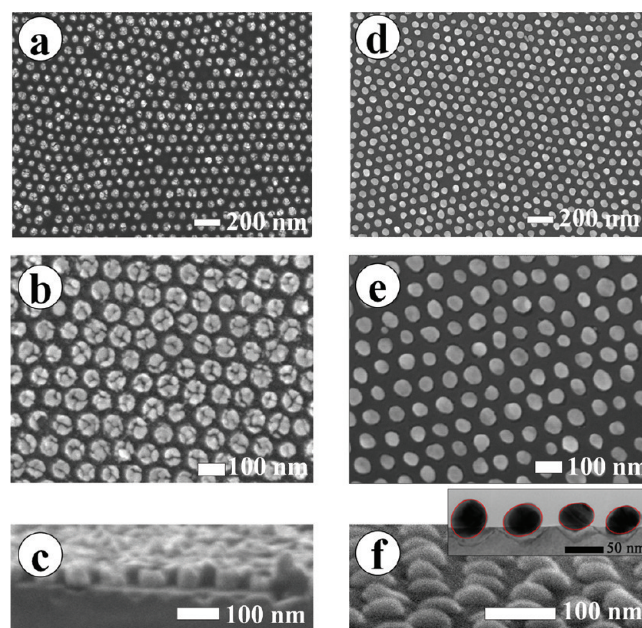

Figure 2. Scanning electron microscopy images of (a−c) Au nanorods and (d−f) nanodiscs measured in (a, b, d, e) top-view and (c,f) cross-section is shown shown in both (a, d) low and (b, e) high magnifications. The inset in (f)shows cross-sectional TEM image of gold nanodiscs revealing an ellipsoidal profile, with the particles slightly buried within the substrate. The outline of the particles is intentionally marked in red to show the ellipsoidal profile better.

nanoparticulate gold structure obtained using electroless process. The discs were found to exhibit a diameter of 55.2 (±4) nm and height of 35.3(±5.4) nm as measured using SEM (Figure 2e,f) and AFM respectively. Cross-sectional TEM measurements further reveal that the discs have an ellipsoidal shape and with a small portion of the particle buried within the substrate

(Figure 2f inset). The height of the particles as measured from the cross-sectional TEM measurements were found to be ~40 nm. The depression below the nanoparticle is presumably formed by substrate etching, due to the presence of HF in the electroless chemical bath. The investigations reported in literature on the use of metal nanoparticles as catalyst for electrochemical etching of Silicon is of interest in this context.[40,41] The transformation from rod to disc was also necessary to ensure stability of the particle arrays during SERS experiments. This is because the nanoparticulate nature of the rods led to loss in pattern arrangement due to capillary forces experienced when exposed to the analyte solution. Although, the disintegration of nanorods can possibly be countered by preserving the PMMA template around the gold nanorods, the arrays that consist of exposed polymers would still suffer from insufficient mechanical stability due to localized heating effects during SERS analysis, or polymer swelling in certain solvents.

The gold electroless growth shown here as taking place with excellent uniformity and fidelity is only an example of what could be readily extended to a range of other processing that depend on selective growth of material from surface. For instance, the electroless process shown above can be directly extended to preparation of silver, platinum, palladium or copper arrays on silicon or other semiconductor surfaces such as Ge, GaAs or GaN.[38,39] Other possibilities include selective growth of polyaniline films[42] or electrodeposition of metals[16] on surface using these templates on a conducting substrate such as gold or ITO. Alternatively, the templates can be used to direct the assembly of nanoparticles through capillary dewetting into the pores. The use of amphiphilic copolymer self-assembly derived NIL molds therefore provides for efficient production of templates to create technologically relevant nanoarrays of diverse materials. This is due to the fact that the choice of the template material, the template thickness or the substrate on which the patterning is carried out is totally independent of the materials or processes used for self-assembly. The approach allows achieving sub-100 nm scale patterns of all kinds shown earlier in literature, only with significant ease, versatility, and high reproducibility.

Theoretical Calculations. Numerical simulations were performed using finite-difference time domain method to predict the plasmonic properties of the nanodisc arrays. The simulations were run by modeling the nanodiscs as monodisperse ellipsoids (a = b = 55 nm and c = 40 nm) with a periodicity of 80 nm. The value for height and diameter of the discs used for the simulations correspond to the mean values determined from the particle size histograms generated from cross-sectional TEM and SEM measurements respectively. The figure 3a elucidates the schematic diagram of the configuration employed in the numerical simulation. The cross-sectional TEM measurements (Figure 2f, inset) reveal that a portion of the ellipsoid is buried within the silicon substrate, and this observation was taken into consideration during the numerical simulation. A perfectlymatched layer is considered at the top and bottom, and periodic boundary condition is considered at the sides in the numerical simulation. The simulations considered a mesh spacing of 2 nm in x, y, and z directions. A plane wave source is employed to excite the sample at normal incidence through the air medium.

The simulations feature two prominent peaks around 420 and 592 nm, respectively (Figure 3b). The broad peak near 420 nm arises due to the diffraction of incident light by a grating formed due to periodic distribution of Au nanoparticles on silicon substrate.[43]The position of this peak conforms to what can be expected based on the condition for first-order Bragg diffraction for periodicity of 80 nm. The lack of prominence of this peak in the experimental spectrum could be ascribed to the diffracted beam not falling within the estimated collection angle of 16.2° for the 15× objective with NA of 0.28 used for our measurements. The simulation on the other hand takes into account all photons in the near-field placing no restriction on the detection angle. Similar observations on grating effect on periodic metal nanoparticle arrays have been reported earlier in literature.[44,45] Further, the lack of long-range order of the array and defects present in the lattice could be additional contributing factors for lack of prominence of this peak.

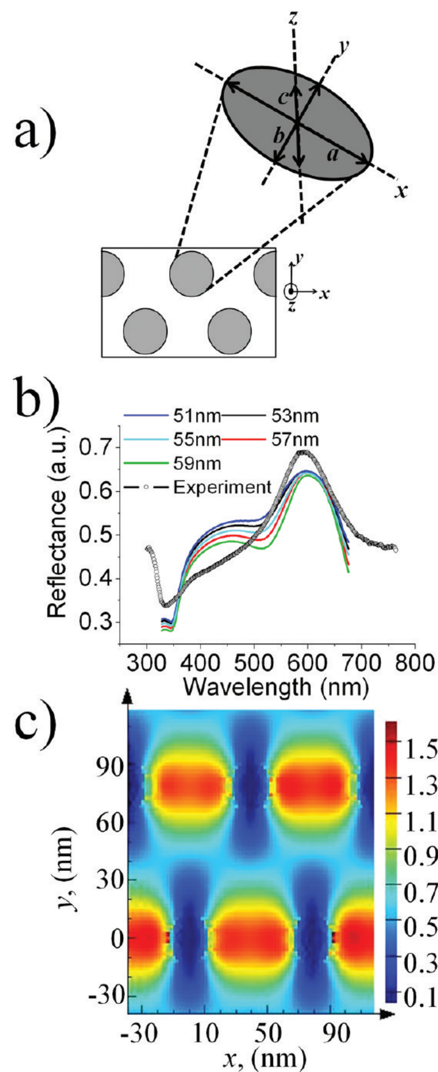

Figure 3. (a) Schematic shows the model consisting of arrays of biaxial gold ellipsoids ($a = b = 55$ nm, c=40 nm) used in simulations. (b) Plot shows comparison between the experimental reflectance spectra with spectra simulated for different ellipsoidal feature widths, maintaining the height of $z = 40$ nm as constant (c) Electrical field intensity profile along (x,y) plane at 633 nm, showing plasmonic coupling between nanodiscs.

The peak at 592 nm is caused due to the plasmon resonance of the ellipsoids. The experimental spectrum is broader in width than the simulated spectra due to distribution of nanoparticle sizes. This is demonstrated by simulating the spectra of gold ellipsoids with systematically increasing in-plane diameter (or

feature widths of 51, 53, 55, 57, and 59 nm) while the height (40 nm) and the periodicity of 80 nm were kept constant. The choice of the values for feature widths in simulations was made by taking into consideration the experimentally observed standard deviation of ~10%. The comparison between the simulated spectra corresponding to different feature widths and the experimental spectra clearly shows the contribution of standard deviation in feature size to the spectral width. The simulation results are in conformity with the experimental and theoretical investigations on ellipsoidal nanoparticle arrays in literature that have shown strong dependence of the plasmon resonance peak position on the ellipsoid's geometric attributes and the substrate used.[46,47] Haynes et al. had earlier observed that the polydispersity in nanoparticle sizes can partly account for the distribution of the LSPR λ_{max}.[48] The observed peak-width for the nanodiscs reflectance is significantly lower than what has been reported for close-packed 2D arrays of colloidal gold particles.[49]

The simulated electrical field intensity profile at the wavelength of SERS excitation, viz. 633 nm, show interparticle plasmonic coupling between nanodiscs (Figure 3c). This can be expected,[50] as the edge−edge separation is only ~25 nm, which is equivalent to the particle radius. Several earlier reports have described enhanced coupling of interparticle plasmon resonance as a function of decreasing particle separation relative to the particle diameter. Such coupling of localized particle plasmon resonance is known to contribute to enhancement in electrical field in the region between the particles.[51] The electrical field intensity and therefore the SERS performance of our arrays can be significantly enhanced by further reducing the separation, and through adequate design and engineering of the feature size and array periodicity. This would necessitate the preparation of silicon molds with fine-tunable feature width and periodicities, for which the employed approach can readily cater to. The ability to precisely simulate the spectral properties is simplified because of the well-defined and narrow distribution of the metal nanopatterns obtained. The usefulness of the simulations has potential to extend far beyond the results shown, toward proposing the suitable choice of array geometries with desired optical properties, thereby enabling fabrication on the basis of rational design principles.

Application as SERS Substrate. The SERS detection performance of nanodisc substrates was found to be promising, as expected from the enhanced electrical field intensities because of strong interparticle coupling. The SERS signal intensities also heavily depends on the molecular characteristics and the nature of interaction exhibited by the molecules with the substrate. Therefore, SERS enhancements shown with a single molecule cannot be readily extrapolated to every other molecule.[52,53]

This is also one of the draw backs in several SERS reports in literature, where the studies use only single type of molecule. To prove the generality of the SERS substrate, the detection of molecules that are both resonant and nonresonant and exhibiting different interaction modes with the substrate is performed in this context. Three different Raman analytes, namely Crystal Violet (CV), Naphthalene thiol (NT) and 1,2-bis pyridyl ethane (BPE) were chosen for the analysis. The molecules were chosen on the basis of their well-characterized chemical and spectroscopic properties as well as their different modes of interaction with the substrate. CV exhibits high Raman cross section with a possibility of resonant interaction with the metal structure at the laser wavelength used.[54] BPE is a nonresonant molecule that is neutral and can physisorb to the substrate by non covalent interactions.[55] NT, also nonresonant, can covalently anchor to

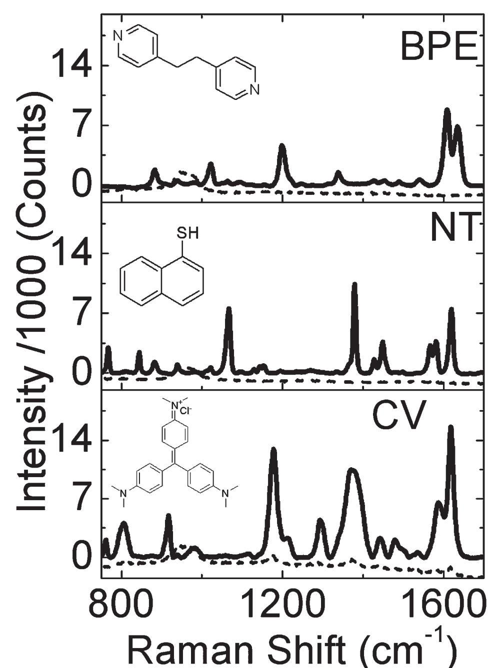

Figure 4. Surface-enhanced Raman spectra (SERS) of BPE (1 mM), NT (10 μM) and CV (1 μM) measured on gold nanodisc arrays are shown to yield spectra with good band resolution and intensity. The spectra of unpatterned gold substrate measured under identical conditions is shown in dotted lines for reference. The spectra were measured using 633 nm laser focused using a 50× objective lens with low laser power of 6.3 mW and short acquisition time of 10 s. Laser spot size used is ~1 μm. The spectra represent an average of 8 accumulations done at random locations on the substrate.

the substrate via thiol groups.[56] Excellent Raman spectra were obtained in all the three cases on the nanodisc arrays exhibiting a good band resolution and intensity (Figure 4) at concentration of the molecules matching with that from literature.[54−56] In each measurement, the average SERS spectra of the molecule is recorded from eight random locations that are at least 3 mm apart. The spectra from the silicon wafer outside the patterned area which has only gold film shows no Raman signals under the given conditions of measurement. Further, as a comparison, we tested the performance of our substrate as against the commercial KlariteTH substrates (see Figure S1 in the Supporting Information).[57] Spectra recorded under the same conditions for all the three molecules revealed that the nanodisc arrays performed far better in terms of signal intensity and spectral resolution (see the Supporting Information for details).

A typical standard deviation of ~10% from the average value of intensity was observed comparing five major peaks of CV molecule. Crystal violet is known to have the highest point to point variation due to its noncovalent interaction with the surface, preferential adsorption to SERS active hotspots and multiple orientations possible on the substrate surface.[58] Hence to have a variation of ~10% for CV is remarkable in terms of SERS reproducibility considering that each measurement is made at least 3 mm apart on the substrate. The Au nanorod arrays (Figure 2a) were also subjected to SERS analysis and were found to produce SERS approximately 30% higher than for the discs. However, analysis of the chips after the SERS experiments revealed that the rods had disintegrated and no longer retained

their form due to their nanoparticulate nature and a poor adhesion to the substrate. We expect that this issue to be common among nanoparticles formed by electrochemical or electro-less deposition processes. This underlines the need to characterize the substrates even after the SERS experiment, which has often been neglected in SERS reports published in literature. The discs however were found to retain their morphological integrity in all cases. Although NIL has been shown before for creating SERS substrates,[16,59] the feature sizes are typically in the submicrometer regime. Our approach benefits from the self-assembly route to NIL molds that allows accessing sub-100 nm feature widths with high density and low fabrication costs. From the absolute values of the SERS signals obtained, the nanodisc arrays presented here are better in their performance with other complex and expensive substrates reported earlier.[52,60,61]

CONCLUSION

In this work, controlled fabrication of high-density arrays of gold nanorods and nanodiscs was demonstrated using novel combination of NIL and copolymer lithography. The approach allows for high-throughput and cost-effective fabrication, in addition to inherent reproducibility due to the reusability of the NIL molds. SERS studies using molecules with different Raman cross section and interaction modes with substrate shows that nanodisc arrays exhibit excellent stability, signal strength and resolution of spectra. The experimentally observed SERS performance is supported by the interparticle plasmonic coupling demonstrated by numerical electromagnetic simulations. Engineering the feature-width and separation between the particles toward maximizing SERS performance by controlling templates used for mold fabrication, and application of these arrays in SERS based biosensing are currently underway. The fabrication protocols shown is of high relevance not only to SERS, but to several other applications where high-resolution patterns are sought as functional components within nanoscale devices for solid-state lighting, data storage, energy generation, energy-storage, sensors, and catalysis.

EXPERIMENTAL SECTION

Pillar Array Fabrication. Silicon pillar arrays were fabricated by pattern transfer of PS-b-P2VP reverse micelles arrays into Si substrates with some modifications to the procedure already reported in literature.[32]In brief, the copolymer reverse micelles were coated from m-Xylene solutions with concentration between 0.6 and 1%w/w on Si substrates consisting of a thermally grown silicon oxide layer of 25 nm thickness. Copolymer micelle coatings were subjected to a brief oxygen plasma to expose the substrate, followed by a first etch into silicon oxide using C_4F_8/CH_4 plasma for 10s duration using AMS 200 DSE, an inductively coupled plasma (ICP) etcher (Alcatel Micromachining Systems, Annecy, France). This was followed by a second etch into silicon using Cl_2 plasma plasma for 30s using STS etcher (Surface Technology Systems, New Port, UK). The residual silicon oxide mask was subsequently removed by immersing the wafers in BHF solution for 1 minute. The silicon pillars were characterized using field emission scanning electron microscope (FESEM) using JSM-6700F microscope (JEOL Ltd. Tokyo Japan).

Nanoimprinting. Mr-I PMMA35k (Microresist Technologies, Germany) was used as a resist that provides a 100 nm thick film when spun at 3000 rpm. The resist was spun at 3000 rpm for 30s followed by imprinting at 150 °C, at 50 bar pressure for 5 min using a Obducat 4 in. imprinter (Obducat, Sweden). The imprinted structures were characterized using FESEM and AFM (Multimode AFM, Digital instruments, CA, USA)

Fabrication and Characterization of Nanorod and Nanodisc Arrays. Gold plating was carried out in a plating bath consisting of a mixture of 2.3 mM $HAuCl_4$/0.9% HF in which the silicon substrate consisting of the nanoporous template was exposed for 1 min. Removal of the polymer template was carried out by exposure to oxygen plasma in a reactive ion etcher (Oxford plasmlab100, Oxford Instruments, UK) at 65 mTorr, 30W, 20 sccm O_2 for 5 min to obtain nascent gold nanorods. The rods were annealed at 200 °C for 2 h to obtain nanodiscs that exhibited a reflectance peak at 592 nm. The reflectance spectra were recorded using UV−visible−NIR microspectrometer (Craic Technologies, CA, USA). The samples were measured on areas of 77 μm × 77 μm using 15× objective with NA of 0.28.

SERS Experiments. For the SERS experiments, the substrates were incubated in the respective analyte solutions in deionized water for overnight. One micromolar Crystal Violet (Sigma-Aldrich), 1 mM BPE, and 10 μM NT were used. The substrates were taken from this solution and placed on a microscopic slide with a coverslip placed on top. The SERS measurements was carried out in backscattering geometry using Raman microscope (Invia, Renishaw, UK) equipped with a line grating (1200 line/mm, spectral resolution at 1 cm^{-1}) and a CCD cooled at −70 °C. A HeNe laser at 633 nm (maximum output at 6.3 mW, Renishaw, UK) with 50X objective (N.A. 0.75, Leica) was used as source. The Raman signal was collected through the same objective in a backscattering geometry. To evaluate the reproducibility of the measurement, the spectra were measured from eight random locations on each substrate. In this study, each spectrum was collected at optical power of 6.3 mW with an integration time of 10 s. The shutter of the laser was immediately closed after each measurement to minimize any possible photo damage on the samples under a prolonged illumination. Baseline correction of the measured spectra was performed to remove the broad fluorescence band for data analysis. The acquired SERS spectra were corrected by subtracting the fluorescence background fitted with a third-order polynomial using the provided software package (Renishaw WiRE version 3.0, Renishaw).[62] Throughout the data analysis, the highest intensity value at Raman stokes shift of 1620 cm^{-1} was used to compare the SERS performance among the substrates treated with CV.

ASSOCIATED CONTENT

Supporting Information. Surface-enhanced Raman spectra (SERS) of CV, BPE, and NT on Klarite substrates (PDF). This material is available free of charge via the Internet at http://pubs.acs.org

AUTHOR INFORMATION

Corresponding Author

*E-mail: krishnamoorthys@imre.a-star.edu.sg (S.K.); praveen@sbic.a-star.edu.sg (P.T.).

ACKNOWLEDGMENT

Funding support received from Joint Council Office (JCO) of the Agency for Science Technology and Research (A*STAR), vide grant 10/3/EG/05/04 is gratefully acknowledged. The authors further thank Dr. Malini Olivo (SBIC) for helpful discussions and support, and Hui Ru Tan (IMRE) for help with TEM cross-section measurements.

REFERENCES

(1) Maier, S. A.; Atwater, H. A. *J. Appl. Phys.* **2005**, *98*, 011101–011111.

(2) Kelly, K. L.; Coronado, E.; Zhao, L. L.; Schatz, G. C. *J. Phys. Chem. B* **2003**, *107*, 668–677.
(3) Jain, P. K.; Huang, W.; El-Sayed, M. A. *Nano Lett.* **2007**, *7*, 2080–2088.
(4) Anker, J. N.; Hall, W. P.; Lyandres, O.; Shah, N. C.; Zhao, J.; Van Duyne, R. P. *Nat. Mater.* **2008**, *7*, 442–453.
(5) Willets, K. A.; Van Duyne, R. P. *Ann. Rev.Phys.Chem.* **2007**, *58*, 267−297.
(6) Sepúlveda, B.; Angelomé, P. C.; Lechuga, L. M.; Liz-Marzán, L. M. *Nano Today* **2009**, *4*, 244–251.
(7) Pieczonka, N. P. W.; Aroca, R. F. *Chemical Soc. Rev.* **2008**, *37*, 946–954.
(8) Nie, S.; Emory, S. R. *Science* **1997**, *275*, 1102–1106.
(9) Lin, X. M.; Cui, Y.; Xu, Y. H.; Ren, B.; Tian, Z. Q. *Anal. Bioanal. Chem.* **2009**, *394*, 1729–1745.
(10) Brown, R. J. C.; Milton, M. J. T. *J. Raman Spectrosc.* **2008**, *39*, 1313–1326.
(11) Wang, Y.; Becker, M.; Wang, L.; Liu, J.; Scholz, R.; Peng, J.; Go sele, U.; Christiansen, S.; Kim, D. H.; Steinhart, M. *Nano Lett.* **2009**, *9*, 2384–2389.
(12) Lu, J.; Chamberlin, D.; Rider, D. A.; Liu, M. Z.; Manners, I.; Russell, T. P. *Nanotechnology* **2006**, *17*, 5792–5797.
(13) Choi, D.; Choi, Y.; Hong, S.; Kang, T.; Lee, L. P. *Small* **2010**, *6*, 1741–1744.
(14) Hsu, C. F.; Wang, K.; Wang, L. *Adv. Mater.* **2006**, *18*, 491–495.
(15) Ruan, C.; Eres, G.; Wang, W.; Zhang, Z.; Gu, B. *Langmuir* **2007**, *23*, 5757–5760.
(16) Yang, B. J.; Lu, N.; Huang, C. Y.; Qi, D. P.; Shi, G.; Xu, H. B.; Chen, X. D.; Dong, B.; Song, W.; Zhao, B.; Chi, L. F. *Langmuir* **2009**, *25*, 55–58.
(17) varez-Puebla, R.; Cui, B.; Bravo-Vasquez, J. P.; Veres, T.; Fenniri, H. *J. Phys. Chem. C* **2007**, *111*, 6720–6723.
(18) Sánchez-Iglesias, A.; Aldeanueva-Potel, P.; Ni, W.; Ramón-Juste, J.; Pastoriza-Santos, I.; Alvarez-Puebla, R. A.; Mbenkum, B. N.; Liz-Marzán, L. M. *Nano Today* **2010**, *5*, 21–27.
(19) Hulteen, J. C.; Treichel, D. A.; Smith, M. T.; Duval, M. L.; Jensen, T. R.; Van Duyne, R. P. *J. Phys. Chem. B* **1999**, *103*, 3854–3863.
(20) Qin, L.; Zou, S.; Xue, C.; Atkinson, A.; Schatz, G. C.; Mirkin, C. A. *Proc. Natl. Acad. Sci.* **2006**, *103*, 13300–13303.
(21) Chou, S. Y.; Krauss, P. R.; Renstrom, P. J. *Science* **1996**, *272*, 85–87.
(22) Guo, L. J. *Adv. Mater.* **2007**, *19*, 495–513.
(23) Chou, S. Y.; Krauss, P. R.; Renstrom, P. J. *Appl. Phys. Lett.* **1995**, *67*, 3114–3117.
(24) Zhou, W.; Zhang, J.; Li, X.; Liu, Y.; Min, G.; Song, Z.; Zhang, J. *Appl. Surf. Sci.* **2009**, *255*, 8019–8022.
(25) Aryal, M.; Buyukserin, F.; Mielczarek, K.; Zhao, X. M.; Gao, J.; Zakhidov, A.; Hu, W. *J. Vac. Sci. Technol., B* **2008**, *26*, 2562–2566.
(26) Yanagishita, T.; Kumagai, N.; Nishio, K.; Masuda, H. *J. Photopolym. Sci. Technol.* **2007**, *20*, 569–571.
(27) Lee, P. S.; Lee, O. J.; Hwang, S. K.; Jung, S. H.; Jee, S. E.; Lee, K. H. *Chem. Mater.* **2005**, *17*, 6181–6185.
(28) Kuo, C. W.; Shiu, J. Y.; Cho, Y. H.; Chen, P. *Adv. Mater.* **2003**, *15*, 1065–1068.
(29) Kuo, C. W.; Shiu, J. Y.; Chen, P. *Chem. Mater.* **2003**, *15*, 2917–2920.
(30) Li, W.; Xu, L.; Zhao, W. M.; Sun, P.; Huang, X. F.; Chen, K. J. *Appl. Surf. Sci.* **2007**, *253*, 9035–9038.
(31) Park, H. J.; Kang, M. G.; Guo, L. J. *Acs Nano* **2009**, *3*, 2601–2608.
(32) Krishnamoorthy, S.; Gerbig, Y.; Hibert, C.; Pugin, R.; Hinderling, C.; Brugger, J.; Heinzelmann, H. *Nanotechnology* **2008**, *19*, 85301–85307.
(33) Hamley, I. W. *Nanotechnology* **2003**, *14*, R39–R54.
(34) Krishnamoorthy, S.; Hinderling, C.; Heinzelmann, H. *Mater. Today* **2006**, *9*, 40–47.
(35) Park, H. J.; Kang, M. G.; Guo, L. J. *Acs Nano* **2009**, *3*, 2601–2608.
(36) Krishnamoorthy, S.; Manipaddy, K. K.; Yap, F. L. *Adv. Funct. Mater.* **2011**n/a.
(37) Krishnamoorthy, S.; Pugin, R.; Brugger, J.; Heinzelmann, H.; Hinderling, C. *Adv. Funct. Mater.* **2006**, *16*, 1469–1475.
(38) Aizawa, M.; Buriak, J. M. *J. Am. Chem. Soc.* **2005**, *127*, 8932–8933.
(39) Aizawa, M.; Buriak, J. M. *Chem. Mater.* **2007**, *19*, 5090–5101.
(40) Huang, Z.; Zhang, X.; Reiche, M.; Liu, L.; Lee, W.; Shimizu, T.; Senz, S.; Go sele, U. *Nano Lett.* **2008**, *8*, 3046–3051.
(41) Tsujino, K.; Matsumura, M. *Adv. Mater.* **2005**, *17*, 1045–1047.
(42) Li, X.; Tian, S.; Ping, Y.; Kim, D. H.; Knoll, W. *Langmuir* **2005**, *21*, 9393–9397.
(43) Yang, L.; Yan, B.; Premasiri, W. R.; Ziegler, L. D.; Negro, L. D.; Reinhard, B. M. *Adv. Func. Mater.* **2010**, *20*, 2619–2628.
(44) Felidj, N.; Aubard, J.; Levi, G.; Krenn, J. R.; Schider, G.; Leitner, A.; Aussenegg, F. R. *Phys. Rev. B.* **2002**, *66*, 245407.
(45) Yan, B.; Thubagere, A.; Premasiri, W. R.; Ziegler, L. D.; Dal Negro, L.; Reinhard, B. M. *ACS Nano* **2009**, *3*, 1190–1202.
(46) Grand, J.; Adam, P. M.; Grimault, A. S.; Vial, A.; Lamy de la Chapelle, M.; Bijeon, J. L.; Kostcheev, S.; Royer, P. *Plasmonics* **2006**, *1*, 135–140.
(47) Kelly, K. L.; Coronado, E.; Zhao, L. L.; Schatz, G. C. *J. Phys. Chem. B.* **2003**, *107*, 668–677.
(48) Haynes, C. L.; Van Duyne, R. P. *J. Phys. Chem. B.* **2001**, *105*, 5599–5611.
(49) Wei, A.; Kim, B.; Sadtler, B.; Tripp, S. L. *Chemphyschem.* **2001**, *2*, 743–745.
(50) Su, K. H.; Wei, Q. H.; Zhang, X.; Mock, J. J.; Smith, D. R.; Schultz, S. *Nano Lett.* **2003**, *3*, 1087–1090.
(51) Gunnarsson, L.; Bjerneld, E. J.; Xu, H.; Petronis, S.; Kasemo, B.; K+ñll, M. *Appl. Phys. Lett.* **2001**, *78*, 802–804.
(52) Brown, R. J. C.; Milton, M. J. T. *J. Raman Spectrosc.* **2008**, *39*, 1313−1326.
(53) Natan, M. J. *Faraday Discuss.* **2006**, *132*, 321–328.
(54) Can amares, M. V.; Chenal, C.; Birke, R. L.; Lombardi, J. R. *J. Phys. Chem. C* **2008**, *112*, 20295–20300.
(55) Fan, J. G.; Zhao, Y. P. *Langmuir* **2008**, *24*, 14172–14175.
(56) varez-Puebla, R. A.; D. S, . D. S., Jr.; Aroca, R. F. *The Analyst* **2004**, *129*, 1251–1256.
(57) Perney, N. M. B.; Garcia de Abajo, F. J.; Baumberg, J. J.; Tang, A.; Netti, M. C.; Charlton, M. D. B.; Zoorob, M. E. *Phys. Rev. B.* **2007**, *76*, 35426.
(58) Kudelski, A. *Chem. Phys. Lett.* **2005**, *414*, 271–275.
(59) Li, Z.; Tong, W. M.; Stickle, W. F.; Neiman, D. L.; Williams, R. S.; Hunter, L. L.; Talin, A. A.; Li, D.; Brueck, S. R. J. *Langmuir* **2007**, *23*, 5135–5138.
(60) Banholzer, M. J.; Millstone, J. E.; Qin, L.; Mirkin, C. A. *Chem. Soc. Rev.* **2008**, *37*, 885–897.
(61) Lai, K.; Zhang, Y.; Du, R.; Zhai, F.; Rasco, B. A.; Huang, Y. *Sens. Instrum. Food Qual. Saf.* **2011**, 1−6.
(62) Yuen, C.; Zheng, W.; Huang, Z. W. *J. Biomed. Opt.* **2008**, *13*.